

1 **Diagnosing the seasonal land-atmosphere correspondence over Northern Australia: Dependence**
2 **on soil moisture state and correspondence strength definition**

3

4

5

6

7

8 **Mark Decker¹ Andy Pitman¹ and Jason Evans¹**

9

10

11

12

13 [1] Climate Change Research Centre and ARC Centre of Excellence for Climate System Science,

14 University of New South Wales

15

16

17

18

19

20

21

22

23

24

25

26

27

28 Correspondence to: Mark Decker (m.decker@unsw.edu.au)

29

30 **Abstract**

31 The strength of the correspondence between the land and the atmosphere during the onset
32 (September) through to the peak (February) of the wet season over Northern Australia is statistically
33 diagnosed using ensembles of offline land surface model simulations that produce a range of different
34 background soil moisture states. We derive correspondence between the soil moisture and the
35 planetary boundary layer via a statistical measure of association. The simulated evaporative fraction
36 and the boundary layer are shown to be strongly associated during both SON and DJF despite the
37 differing background soil moisture states between the two seasons and among the ensemble members.
38 The sign and magnitude of the boundary layer-surface layer soil moisture association during the onset
39 of the wet season (SON) differs from the correspondence between the evaporative fraction and
40 boundary layer from the same season, and the correlation between the surface soil moisture and
41 boundary layer [association coupling](#) during DJF. The patterns and magnitude of the surface flux-
42 boundary layer correspondence are not captured when the relationship is diagnosed using the surface
43 layer soil moisture alone. The conflicting results arise because the surface layer soil moisture lacks
44 strong association with the atmosphere during the monsoon onset because the evapotranspiration is
45 dominated by transpiration. Our results indicate that accurately diagnosing correspondence and
46 therefore coupling strength in seasonally dry regions, such as Northern Australia, requires root zone
47 soil moisture to be included.

48

49 1 Introduction

50

51 The land surface influences the atmosphere at multiple spatial and temporal scales (Pitman
52 2003; Pielke et al., 2011; Williams and Maxwell, 2011). Land-atmosphere coupling strength is the
53 degree to which land surface anomalies (e.g. soil moisture, vegetation characteristics, temperature,
54 snow cover) lead to changes in atmospheric states and fluxes (e.g. rainfall, cloud cover, moisture
55 convergence) as well as how anomalies in the atmosphere affect the land surface. The influence of
56 land surface anomalies on atmospheric anomalies (and vice versa) proceeds through a chain of non-
57 linear processes. The strength of these processes varies spatially and temporally and depend, in part,
58 on the background state of the system (Betts 2004; Koster and Suarez, 2003; Taylor and Ellis 2006).
59 The chain of mechanisms between soil moisture (SM) and precipitation (P) anomalies can be
60 summarized following Santanello et al. (2011) as

$$61 \quad \Delta SM \Rightarrow \Delta EF_{SM} \Rightarrow \Delta PBL \Rightarrow \Delta EF_{ATM} \Rightarrow \Delta CLD \Rightarrow \Delta P \quad (1)$$

62 where the changes in soil moisture (ΔSM) lead to changes in evaporative fraction (ΔEF_{SM}), which
63 alters the properties of the planetary boundary layer (ΔPBL) including the state (temperature,
64 humidity) and the entrainment rate. These three near surface coupling mechanisms ($\Delta SM, \Delta EF_{SM}$, and
65 ΔPBL) precede changes away from the land surface that further change evaporative fraction (ΔEF_{ATM}),
66 leading to changes in cloud development and growth (ΔCLD), and ultimately forcing changes in
67 precipitation (ΔP). The chain cycles with ΔP driving ΔSM to varying degrees depending on the region
68 and season (Zhang et al. 2008). Equation (1) is a conceptualization of complex and nonlinear
69 processes, such that the sign of the ΔCLD response to a ΔSM forcing can vary (Westra et al. 2012;
70 Gentine et al. 2013). Equation (1) is a simplification of the short (less than a day) timescale coupling
71 mechanisms and neglects large scale circulation and moisture feedbacks (Lee et al. 2012; Lintner and
72 Neelin 2009; Lintner et al. 2013). Additional feedbacks that operate on short timescales not shown in
73 (1), such as ΔEF_{SM} or ΔEF_{ATM} leading to ΔSM , may also be important (Seneviratne et al. 2010; Meng
74 et al. 2014a,b). Despite simplifications, Equation (1) highlights the primary control SM exerts on EF
75 as compared to secondary factors such as entrainment (Gentine et al. 2011). In a convective regime
76 ΔSM initiates a series of events that first alter the atmosphere (ΔPBL) prior to changing P. The series

77 of events from $\Delta SM - \Delta PBL$ comprises the terrestrial portion of the coupling mechanisms and is the
78 focus of this study, with coupling examined here limited to these processes. The ΔSM through ΔPBL
79 sequence is a necessary, but not sufficient, set of processes that determine how P responds to changes
80 in SM.

81
82 The sensitivity of atmospheric processes to ΔSM has been quantified with observations (Koster
83 et al. 2003; Taylor and Ellis 2006) and multiple model experiments (Dirmeyer et al. 2006; Guo et al.
84 2006; Hirsch et al. 2013; Koster et al. 2000; Koster et al. 2006; Koster et al. 2011; Lee et al. 2012).
85 Ferguson et al. (2012) combined multiple sources of reanalysis data with LCL and SM observations to
86 examine the relationship between early morning surface layer SM (SM_1), and both the lifting
87 condensation level (LCL) and the EF in the afternoon during the convective season. The relationship
88 was quantified using the Kendall tau coefficient ($K\tau$), a non-parametric rank correlation coefficient
89 that measures the association between two time series. Ferguson et al. (2012) found strong coupling
90 ($K\tau$) between SM_1 -EF, EF-LCL, and SM_1 -LCL over many regions including monsoon regions such as
91 Northern Australia. These three coupling mechanisms span the first three components in Equation (1)
92 (ΔSM , ΔEF_{SM} and ΔPBL). While these represent only part of the processes involved in land-
93 atmosphere coupling, they comprise a fundamental pathway by which SM anomalies drive an
94 atmospheric response.

95
96 Several regional analyses have investigated the importance of land-atmosphere coupling in
97 Northern Australia (Evans et al. 2011). Koster et al. (2000) showed land-atmosphere coupling
98 increased the variance of P in both Northern and Eastern Australia. In agreement, Ferguson et al.
99 (2012) found high correlations in SM_1 -EF, EF-LCL, and SM_1 -LCL during the convective (monsoon)
100 season over the Northern savannas. These studies were limited in scope and did not explicitly explore
101 how the coupling behaves during periods with different background climate states.

102
103 To examine land-atmosphere coupling strength we explore the correspondence between model
104 derived soil moisture and water flux estimates with the observation based estimates of the boundary
105 layer state. Significant association between soil moisture or surface fluxes and the atmosphere

106 provides a necessary but not sufficient condition to demonstrate significant land-atmosphere coupling.
107 The lack of land-atmosphere feedbacks in offline simulations means we cannot assess cause and
108 effect, but by examining the statistical correspondence we can determine if the system states coevolve
109 in a manner consistent with strong coupling. We focus on Northern Australia to examine whether the
110 correspondence between soil moisture and the boundary layer can be diagnosed from SM_1 in regions
111 with a pronounced dry season, given the influence of groundwater on transpiration and deep SM
112 variability (Decker et al. 2013). Northern Australia has a pronounced May to September dry season
113 and a monsoon-driven wet season from November through February (Figure 1). The monsoonal
114 climate allows us to examine the SM_1 -LCL association as defined in Ferguson et al. (2012) in sharply
115 contrasting seasons (Figure 1) that exhibit contrasting background soil moisture states. By examining
116 the differences between correspondence during the onset (defined here as SON to coincide with the
117 initial increase in rainfall) of the wet season when soil moisture will be low, and then through to the
118 peak (defined as DJF to coincide with the precipitation maximum) of the wet season, we aim to
119 determine the reliability of diagnosing the terrestrial and near surface stages of land-atmosphere
120 correspondence using $K\tau$ derived from SM_1 and LCL during periods where total ET fluxes are
121 dominated by either soil evaporation or transpiration. The statistical association is defined here such
122 that the land surface processes in Equation (1) (ΔSM , ΔEF_{SM} and ΔPBL) are examined, while the
123 sequence of events in the atmosphere (ΔCLD and ΔP) are neglected. This terrestrial derived statistical
124 association captures how ΔSM relates to state changes in the mixed layer (ΔPBL). Strong association
125 as defined here is a necessary but not sufficient prerequisite for strong ΔSM - ΔP coupling. An
126 ensemble of offline simulations using two model configurations, one of which neglects groundwater
127 and therefore contains greatly reduced deep soil moisture, are driven using four forcing datasets. The
128 simulations provide estimates of SM_1 in addition to SM over the root zone (SM_{rz}), total ET and the ET
129 components. Afternoon (2 pm local time) LCL is derived using the near surface atmospheric variables
130 from the forcing datasets, and the sensitivity of the ensemble median $K\tau$ is examined for the onset and
131 peak of the monsoon season.

132

133 This manuscript is organized as follows. The model simulations, the SM_1 and ET observations
134 used for model evaluation, and the near surface atmospheric datasets are summarized in Section 2.

135 Section 3 outlines the statistical measure used to define the association between the different states of
136 association used for coupling strength, the derivation of LCL from the atmospheric data, and the
137 model experiments used to estimate the evaporative fraction and soil moisture. The Results section
138 consists of the SM₁-LCL and EF-LCL based association strength, the impact of defining association
139 strength with SM_{rrz} (the root zone SM) are presented in Section 4. The results are explained in terms
140 of the governing physical processes and previous research in Section 5.

141

142 **2 Model Simulations and Data**

143 **2.1 Near Surface Atmospheric and Forcing Data**

144 The lifting condensation level (LCL see Section 3.2) over the entire study region is computed
145 from combinations of near surface atmospheric data using two reanalysis products. The LCL is also
146 calculated at the two flux sites using the tower observations. The model simulations (see Section 2.2)
147 are driven using a combination of atmospheric states and fluxes from reanalysis products, a gauge
148 based daily precipitation dataset, and a 3 hourly satellite-based precipitation product. We follow
149 Decker et al. (2014) and utilize four forcing datasets to drive model simulations.

150

151 The two gridded sources of temperature, humidity, wind speed, pressure, and radiative fluxes
152 are the Global Land Data Assimilation System (GLDAS, [http://disc.sci.gsfc.nasa.gov/hydrology/data-](http://disc.sci.gsfc.nasa.gov/hydrology/data-holdings)
153 [holdings](http://disc.sci.gsfc.nasa.gov/hydrology/data-holdings), Rodell et al., 2004) and the Modern-Era Retrospective Analysis for Research and
154 Applications (MERRA) product (Bosilovich et al., 2008). These two datasets are utilized due to the
155 high spatial resolution of GLDAS (0.25°) and high temporal resolution of MERRA (hourly). Two
156 forcing datasets are comprised of the uncorrected GLDAS and MERRA data interpolated to a common
157 0.25° x 0.25° grid. In addition two precipitation corrected datasets developed in Decker et al. (2014)
158 are used. The uncorrected atmospheric states and radiative fluxes from MERRA are combined with P
159 corrected via two algorithms. First, MERRA is corrected using the Australian Water Availability
160 Project (AWAP) daily gridded precipitation data (Jones et al. 2009) to remove the monthly biases
161 (labelled MERRA.B). Second, the MERRA precipitation is replaced with precipitation derived from
162 disaggregating the daily AWAP data with the 3 hourly Tropical Rainfall Measuring Mission (TRMM)
163 3B42 (Huffman et al. 2007) data (labelled MERRA.BT). These two corrected datasets have identical
164 monthly mean precipitation but different distributions of sub-monthly precipitation.

165

166 **2.2 Simulated estimates of Soil Moisture and Evaporative Fraction**

167 We use the community land model version 4 (CLM4, Oleson et al. 2010) to simulate the states
168 and fluxes of water and energy using configurations documented in Decker et al. (2013; 2014). The
169 land surface model simulations and reanalysis products allow for the terrestrial leg ($\Delta SM - \Delta PBL$ in
170 Equation (1)) to be explored explicitly. A detailed description of the groundwater configurations and
171 modifications are given in Decker et al. (2014).

172

173 The suite of simulations is utilized to address forcing data and model configuration
174 uncertainties in addition to exploring a large soil moisture state space. Two different configurations of
175 CLM4 are used. The first consists of the default CLM4 (referred to as CTRL). The second (referred
176 to as DRY) uses a modified CLM4 that replaces the two-way soil moisture coupling between the soil
177 column and the aquifer with a free drainage bottom boundary condition. The modifications
178 significantly reduce the soil moisture at depths below several centimeters and the ET flux during
179 periods of low rainfall while not imparting large differences on the changes in total column water
180 (Decker et al. 2014). The two model configurations thus enable the coupling between the atmosphere
181 and the land surface to be examined under two differing background soil moisture states.

182

183 The CLM4 evapotranspiration is computed as the sum of the soil evaporation, the canopy
184 evaporation and the transpiration. Transpiration is determined from the rate of photosynthesis and is,
185 in part, a function of SM. The dependence on SM is determined by the soil water potential in each
186 soil layer, the root distribution (prescribed by plant functional type, PFT), and the PFT dependence on
187 water stress. The spatial distribution and phenology of PFTs are specified and identical across all
188 simulations. The C3 grass PFT sets approximately 99% of the roots within 1m of the surface, while
189 approximately 90% of the roots are within this depth for the broadleaf evergreen forest PFT.

190

191 The experiment design follows the simulations outlined in Decker et al. (2014) that have been
192 shown to be in good agreement with observations over parts of Australia. One control (CTRL)
193 simulation and one dry simulation are equilibrated for the period 1948-1979 using the corrected
194 NCEP/NCAR data (Qian et al. 2006) after interpolating to the same $0.25^\circ \times 0.25^\circ$ grid as the other

195 forcing datasets. The CTRL and DRY simulations ending in 1979 provide initial conditions for the
196 four CTRL and four DRY simulations from 1979-2007. The model evaluation period spans the five
197 years coincident with the SM and ET data from 2003-2007. The associations are computed using the
198 period 1990-2008. Both the CTRL and the DRY simulations are forced with the four forcing datasets
199 (see Section 2.1): GLDAS, MERRA, MERRA.B, and MERRA.BT, generating a total of eight model
200 simulations. The SM (from all model layers), and turbulent energy fluxes are output at three hourly
201 intervals (coincident with the temporal resolution of the GLDAS forcing), while the remaining CLM4
202 output is saved as monthly means.

203

204 **2.3 Validation Data: Soil Moisture and Evapotranspiration**

205 The spatial-temporal behavior of the simulated surface soil moisture (SM_1) and
206 evapotranspiration (ET) are validated against gridded observationally based estimates. SM_1 is
207 evaluated against the daily Advanced Microwave Scanning Radiometer-Earth Observing System
208 (AMSR-E) L3 surface SM product. The data are derived from passive microwave measurements and
209 available for the period 2002 to 2011 (Njoku et al. 2003). AMSR-E based SM compares favorably
210 with in-situ measurements over Australia (Draper et al. 2009) and exhibits spatiotemporal variability
211 consistent with land model simulations (Liu et al. 2009). To simplify the comparison with the
212 simulated SM, the first model layer (~ 0.7 cm deep) SM is assumed comparable to SM from AMSR-E
213 despite the uncertain effective measurement depth (approximately 1 cm) that varies with SM.

214

215 The simulated evapotranspiration is evaluated against three ET products. Multiple ET datasets
216 based on different methodologies are included due to the uncertainty associated with deriving gridded
217 moisture flux data (Jimenez et al. 2011). The Global Land Evaporation Amsterdam Methodology
218 (GLEAM) (Miralles et al. 2010), the model-tree ensemble based dataset from MPI-Jena (J2010
219 hereafter) (Jung et al. 2010), and the Moderate Resolution Imaging Spectrometer (MODIS) MOD16
220 dataset (Mu et al. 2007; 2011) are used to estimate the observed mean seasonal ET fluxes. The
221 observed ET is estimated using the arithmetic mean of the three datasets after the GLEAM and
222 MOD16 data are aggregated to the coarse resolution ($0.5^\circ \times 0.5^\circ$) of the J2010 data. The simulations
223 are subsequently compared to the mean observed ET separately for the wet (December-February) and
224 the end of the dry (September-November) seasons.

225

226 In addition to the gridded SM and ET datasets the model is evaluated against observations
227 from two flux tower sites included in the OZ Flux network (ozflux.org.au). The Adelaide River site
228 (Beringer, 2013a) spans November 2007 through May 2009 and is located at 13.08°S 131.12°E. The
229 Howard Springs site (Beringer, 2013b) spans 2001 to present and is located at 12.48°S 131.15°E. Both
230 sites provide air temperature, water vapor, surface pressure, radiation, turbulent fluxes (including ET),
231 and soil moisture measurements at 30 minute intervals. The level 3 (L3) quality controlled data were
232 utilized in this study. Adelaide River provides SM data at 5cm depth while Howard Springs provides
233 SM at a depth from 10cm. The simulations are validated against the observed ET and SM at these two
234 locations.

235

236 **3 Methods**

237 **3.1 Kendall τ**

238 We evaluate the land-atmosphere coupling strength using Kendall tau ($K\tau$), a non-parametric,
239 rank correlation statistic (Press et al. 1992). Following Ferguson et al. (2012), $K\tau$ is used to indicate
240 the correspondence between two states important to land-atmosphere coupling. $K\tau$ does not assume
241 linearity between the variables being compared and tests for statistical significance. $K\tau$ ranges from -1
242 to 1 (positive values indicate the temporal variations are synchronized), with statistical significance
243 depending on the sample size (approximately 0.12 for the simulation based results in this study). $K\tau$ is
244 defined as

$$245 \quad K_{\tau} = \frac{N_o - N_d}{0.5n(n-1)} \quad (2)$$

246 where N_o is the number of ordinate pairs, N_d is the number of disordinate pairs, and n is the number of
247 observations. Ordinate pairs are pairs of numbers for which the change between them have the same
248 sign, i.e. both are either positive or negative. The strong seasonal cycle in Northern Australia (Figures
249 2 and 3) necessitates that the seasonality be removed from the data or it will likely control the
250 statistical relationship. The least squares linear trend is removed from the data by calculating the trend
251 data are necessarily detrended separately over each season individually. The data are detrended
252 instead of removing the monthly mean annual cycle to ensure we don't create discontinuities within a

253 season. Removing the mean annual cycle could possibly subtract very different mean values from
254 points that are continuous in time, causing artificial discontinuities between the data from last day of a
255 month and the first day of the subsequent month. Detrending the data over a season ensures the
256 methods don't introduce artificial discontinuities between months within a given season~~prior to~~
257 ~~deriving $K\tau$ to prevent the strong seasonal cycle (Figures 2 and 3) from controlling the statistical~~
258 ~~relationship~~. The spatially distributed $K\tau$ is calculated between the seasonally detrended three hourly
259 modeled SM_1 during the morning and the estimated three hourly LCL from the afternoon at each grid
260 cell for each month during both the wet and dry seasons. $K\tau$ is additionally derived with detrended
261 data at two flux tower sites using measurements of SM and LCL estimated from the tower data. The
262 morning SM_1 is utilized because SM will be highest in the morning prior to decreasing during the day
263 due to ET. The local time of SM and LCL varies because the simulations and forcing data utilize
264 GMT. The distributed $K\tau$ is found separately for each of the eight simulated (See Section 2.2)
265 estimates of SM_1 and the four estimates of LCL (Section 3.2), generating a total of 32 estimates of
266 $K\tau$ for each month in both the wet and dry seasons. The median $K\tau$ is found separately for the wet and
267 dry seasons for the two different model configurations (Section 3.3) to give the final estimation of the
268 correspondence. The association is also diagnosed using $K\tau$ between the model simulated afternoon
269 evaporative fraction and the afternoon LCL. A second definition of association is found by calculating
270 $K\tau$ between the morning time root zone SM (SM_{rz}) and the afternoon LCL (SM_{rz} -LCL). SM_{rz} is
271 defined as the vertically averaged SM from the surface to a depth of 1m.

272 The physical meaning of a negative SM-LCL $K\tau$ association is as follows. A high value of SM
273 will cause a larger ET flux, moistening the lower atmosphere, causing a lower LCL. Thus we
274 hypothesis that in regions where the land-atmosphere are coupled the SM-LCL $K\tau$ should be negative.
275 If SM has no association with LCL than $K\tau$ is expected to be statistically insignificant. Similarly, if ET
276 is negatively associated with LCL ($K\tau < 0$), it means that high ET may be moistening the lower
277 atmosphere again leading to a lower LCL.

278

279 **3.2 Calculation of Lifting Condensation Level**

280 The state of the convective atmosphere is evaluated using the lifting condensation level (LCL),
281 defined as the height (in pressure) that a parcel reaches saturation when ascending adiabatically from

282 the surface. While a lower LCL is favorable to convection, it is not a sufficient constraint to guarantee
 283 it. For convection to occur a parcel must reach the level of free convection (LFC), which may not
 284 occur even if a parcel reaches the LCL. The height (in pressure) of the LCL is derived using only near
 285 surface variables under the assumption that the boundary layer is well developed and therefore well
 286 mixed. Estimating the LCL from near surface variables provides heights comparable to direct
 287 observations (Ferguson and Wood 2009). Under these assumptions, the pressure at the LCL is given
 288 by

$$LCL = P_{srf} - P_{srf} \left(\frac{T_{air}}{T_{dew}} \right)^{\frac{-c_p}{R}} \quad (3)$$

289 where P_{srf} is the surface pressure (Pa), T_{air} is the near surface air temperature (K), T_{dew} is the near
 290 surface dew point temperature (K), R is the specific gas constant of dry air ($J K^{-1} kg^{-1}$), and c_p is the
 291 specific heat of dry air at constant pressure ($J K^{-1} kg^{-1}$). Four spatially explicit estimates of LCL are
 292 found by applying Equation (4) to several combinations of near surface forcing data, and two point
 293 wise estimated are derived from the flux tower data. While P_{srf} and T_{air} are directly provided by both
 294 reanalysis products and the tower measurements, T_{dew} is calculated using the available near surface
 295 atmospheric states. The four distributed estimates of LCL are calculated with Equation (4) by: 1)
 296 using GLDAS for pressure and both temperatures, 2) using MERRA for pressure and both
 297 temperatures, 3) using pressure from MERRA and temperatures from GLDAS, and 4) using pressure
 298 from GLDAS and temperatures from MERRA. The LCL is quality controlled by limiting LCL to be
 299 less than the surface pressure.
 300
 301
 302

303 4. Results

304 4.1 Validation of Simulated Soil Moisture and Evapotranspiration

305 The two model configurations are separately validated against the observationally estimated
 306 soil moisture and evapotranspiration on monthly and seasonal timescales, respectively. Figure 2a
 307 shows the timeseries of the area averaged (10-15S to 120-150E) normalized ensemble mean first layer
 308 soil moisture from the CTRL and the DRY ensembles and the AMSR-E observed data. The simulation
 309 dynamics are evaluated using the normalized SM_1 due to the difficulties in direct comparison of

310 simulated and observed soil moisture (Koster et al. 2009). The strong seasonal cycle of soil moisture
311 owing to the monsoonal climate is evident in both the observationally based estimates and the
312 simulations. CTRL and DRY are nearly identical aside from the dry season in 2005 where the soil
313 moisture in CTRL decreases more than that from DRY. The observed moistening of the soil following
314 the dry seasons in Figure 2a occurs within a month to that of the simulated moistening. The mean
315 monthly soil moisture closely follows that of the observationally based estimates and exhibits dynamic
316 behavior independent of the model configuration.

317

318 The bias of the ensemble mean time averaged surface layer soil moisture from the eight
319 simulations against the AMSR-E product is shown in Figure 2b. Over large regions of Northern
320 Australia, the simulated SM_1 is within $0.025 \text{ mm}^3 \text{ mm}^{-3}$ of AMSR-E. The difference in mean SM_1
321 between the two model configurations is similarly small (figure not shown). Figure 2 demonstrates
322 that the temporal evolution (Figure 2a) and mean state (Figure 2b) of the simulated SM_1 are similar to
323 the AMSR-E estimates.

324

325 The seasonal mean ET is validated against the arithmetic mean of the three gridded ET
326 products for both DJF (Figures 3a, 3c, and 3e) and SON (Figures 3b, 3d, and 3f). The observed DJF
327 ET (Figure 3e) has a strong north-south gradient with a maxima centered around 13°S - 130°E . The
328 strong north-south gradient is also present in the ensemble mean ET (Figure 3a), however the
329 simulations overestimate DJF ET over much of the domain. The observationally based estimates
330 show an ET of less than 50 Wm^{-2} south of 18°S while the simulations remain above 60 Wm^{-2} in this
331 region. The mean SON ET is markedly lower compared to DJF ET in both the gridded data (Figure
332 3f) and the simulations (Figure 3b). Similar to DJF, both the model and the ET product show a strong
333 north-south gradient. The simulations underestimate the ET in the York Peninsula (East of 140°E and
334 North of 17°S) during SON and overestimate the ET in this region during DJF. The overestimation of
335 DJF ET compared to the gridded product is much more pronounced for the CTRL simulations (Figure
336 3a) than the DRY simulations (Figure 3c). The underestimation of the SON ET in the simulations is
337 largely a result of including the DRY model configuration. The CTRL simulations exhibit a 10-20
338 Wm^{-2} increase in SON ET over the DRY model runs (Figure 3b and Figure 3d). Overall, the model
339 exhibits spatial-temporal ET in close agreement with this gridded ET product.

340

341 Point measurements of SM and ET at two locations show reasonable agreement with the model
342 simulations. The Howard Springs SM observations 10cm depth (Figure 4a) typically increases from
343 0.05 to 0.2 $\text{mm}^3\text{mm}^{-3}$ from the dry to the wet season. The observations are drier during the wet season
344 and have a smaller (by a factor of two) seasonal cycle than both the DRY and CTRL simulations.
345 DRY is much drier ($\sim 0.08 \text{ mm}^3\text{mm}^{-3}$) than CTRL ($\sim 0.18 \text{ mm}^3\text{mm}^{-3}$) during the dry season and in
346 better agreement with the measurements ($\sim 0.05 \text{ mm}^3\text{mm}^{-3}$). This contrasts with the agreement at the
347 Adelaide River site (Figure 4b) where the measurements and CTRL peak around $0.30 \text{ mm}^3\text{mm}^{-3}$
348 during the 2008 wet season. DRY ($0.02\text{-}0.07 \text{ mm}^3\text{mm}^{-3}$) is again much drier than CTRL (0.15
349 $\text{mm}^3\text{mm}^{-3}$) during the 2008 dry season but CTRL is in better agreement with the data ($0.15 \text{ mm}^3\text{mm}^{-3}$
350 3). The AMSR-E estimate, CTRL, and DRY are similar in Figures 4a and 4b (the Y-axis scale is the
351 same in both figures), while the SM observations at the two sites differ drastically. The disagreement
352 in the mean as well as the amplitude of the seasonal variability is likely due to both the difference in
353 scale between the measurements and simulations and poor representation of soil properties in the
354 model. When the SM comparison is normalized using the first two moments as in Figure 2a (not
355 shown) there is greater agreement between the measurements, AMSR-E, and the simulations.

356

357 The ET data at Howard Springs (Figure 4c) demonstrates that the CTRL simulation always
358 produces too little ET during the dry season. While the gridded ET estimate in Figure 4c falls within
359 10 Wm^{-2} of the CTRL simulation during the dry season, the tower data are nearly 20 Wm^{-2} greater than
360 both during the 2007 and 2008 dry seasons. The wet season peak in ET is well simulated by both
361 CTRL and DRY at Howard Springs. The model performance is different at Adelaide river as both
362 CTRL and DRY have a wet season peak ET of around 120 Wm^{-2} while the measurements peak closer
363 to 150 Wm^{-2} . Figure 4d further demonstrates that DRY has too little dry season ET.

364

365 The results from Figures 2, 3 and 4 demonstrate that CLM4 simulates the monthly and
366 seasonal first layer soil moisture and evapotranspiration reasonably. While the details of the model
367 performance vary depending on which site, season, and ensemble member is used for validation,
368 overall the spatial and temporal patterns of ET and SM are generally captured by the modeling system.
369 The accuracy of the estimated land surface states and fluxes therefore enables the use of the simulated

370 variables in the diagnoses of the land-atmosphere association strength during SON and DJF.

371

372 4.2 Background SM state

373 The sharp contrast in background SM state can be illustrated by taking a spatial-temporal
374 average of SM as a function of depth for CTRL and DRY for DJF (Figure 5a) and SON (Figure 5b).
375 The soil moisture away from the surface is markedly different between CTRL and DRY. During DJF,
376 CTRL shows a slight increase in soil moisture with depth, reaching a peak of $\sim 0.35 \text{ mm}^3 \text{ mm}^{-3}$ at
377 depths near 3 m. In contrast, DRY has a peak soil moisture of only $\sim 0.24 \text{ mm}^3 \text{ mm}^{-3}$ at the surface and
378 decreases with depth to near zero at 3 m. Similar patterns of SM with depth are seen over SON,
379 however SM_1 is considerably lower for both CTRL and DRY compared to DJF.

380

381 Despite the similar mean and temporal behavior of SM_1 shown in Figure 2, SM away from the
382 surface differs substantially between the two model configurations (Figure 5b). The mean DJF ET is
383 similar between CTRL and DRY, with differences between the two only $10\text{-}20 \text{ Wm}^{-2}$, corresponding to
384 roughly 10-20% of the mean value. The fractional contribution of transpiration to the total ET during
385 DJF is roughly 10-30% for both DRY and CTRL (Figure 6 ~~figure not shown~~) indicating that the
386 evaporation is the dominant ET mechanism. The enhanced mean SM in CTRL causes the CTRL ET
387 to be greater than the DRY ET during DJF, yet both compare reasonably reasonable well to the
388 observationally based estimates (Figure 3). However the lack of SM at depths below several
389 centimeters for DRY during SON causes the reduced ET as compared to CTRL during this period.
390 The mean ET during SON is sensitive to the mean SM away from the surface, indicating that
391 transpiration significantly contributes to the total ET during this period as can be seen in Figure 6.
392 The large contribution of transpiration to the total ET in CTRL (Figure 6b) is facilitated by the moist
393 subsurface soil moisture (Figure 5b). The reduced root zone SM in DRY leads to an increase in water
394 stress and reduced transpiration, causing both the lower mean ET and transpiration fraction in DRY
395 relative to CTRL. This reduction during SON is large relative to the mean ET during the period
396 (Figure 3).

397

398 4.3 Correspondence: EF-LCL and SM_1 -LCL

399 The statistical association between the evaporative fraction and the LCL is shown in Figure 76,

400 with the results from the two flux towers shown in enclosed squares around 13°N and 131°E. The
401 insignificant associations are greyed out while the statistically significant results are shown in color.
402 During DJF, CTRL (Figure 7a6a) and DRY (Figure 7c6e) exhibit strong surface flux-atmosphere
403 correspondence, with the strongest association over the Cape York Peninsula (East of 140°E and North
404 of 17°S) and the Southwestern part of the domain. Similarly, the EF-LCL ~~association~~ coupling is
405 significant during SON (Figures 7b and 7d6b and 6d) over much of the domain, although the
406 magnitude is reduced relative to DJF. Both ensembles show strong associations independent of the
407 season, however the differences between CTRL and DRY vary with season. The DJF EF-LCL
408 correspondence near 15°S 132°E is statistically significant in DRY (Figure 7c6e) but not in CTRL
409 (Figure 7a6a), contrasting the similar SON EF-LCL association in this region exhibited by both DRY
410 (Figure 7d6d) and CTRL (Figure 7b6b). The flux towers (boxed squares in Figures 7a-7c6a-6e) both
411 show statistically significant association between EF and the LCL during both seasons. The EF-LCL
412 correspondence from the tower observations agree more closely with DRY in DJF as CTRL show
413 statistically insignificant association in the region (13°S 131°E). The reduced deep layer soil moisture
414 resulting from the removal of the groundwater module enhances the DJF correspondence in agreement
415 with the tower data.

416

417 Figure 87 shows the median Kendall tau ($K\tau$) between SM_1 and the LCL (see Section 3.3) for
418 CTRL and DRY separately during DJF (Figures 8a and 8c7a and 7e) and SON (Figures 8b and 8d7b-
419 and 7d). Several important features are present in Figure 87. The SM_1 -LCL association during DJF
420 and SON is largely similar between the two model configurations. CTRL (Figure 8a7a) and DRY
421 (Figure 8c7e) exhibit similar spatial patterns and magnitudes of $K\tau$. Some regions (17°S 126°E)
422 exhibit increases in the magnitude of $K\tau$ in CTRL relative to DRY in DJF (Figures 8a and 8c7a and
423 7e) although the differences are statistically insignificant over most of the domain. Regardless of these
424 slight variations in $K\tau$, CTRL and DRY exhibit a strong association between SM_1 and the boundary
425 layer during the peak of the wet season over coincident parts of the domain. Both model
426 configurations also show areas (15°S 131°E) with insignificant correspondence adjacent to the strongly
427 associated regions. In contrast, CTRL and DRY both contain regions of significant positive $K\tau$
428 demonstrating a negative correspondence during SON, in disagreement with the results from the

429 Adelaide River tower site. The tower sites both show statistically significant negative SM-LCL
430 association during DJF adjacent to a region (15°S 131°E) of insignificant correspondence both
431 simulations. The similarity in SM₁-LCL correspondence between CTRL and DRY during both DJF
432 and SON implies a similar temporal variability of SM₁ as related to the LCL. From Figure 3, the
433 mean ET fluxes are considerably different during SON. The similar temporal behavior relative to the
434 LCL for both DRY and CTRL indicates that the SM₁ variability is physically independent of the season
435 mean ET fluxes.

436
437 Contrasting Figures [7 and 86-and-7](#) reveals that the surface fluxes (Figures [7b and 7d6b-and-](#)
438 [6d](#)) are associated with the LCL despite the simulated surface layer soil moisture (Figures [8b and 8d7b](#)
439 [and-7d](#)) lacking similar correspondence. The regions of positive $K\tau$ in Figure [87](#) contradict the
440 strongly negative $K\tau$ in Figure [76](#) during SON. The flux towers show negative association for both
441 EF-LCL and SM-LCL during DJF and SON in Figures [7 and 86-and-7](#). The EF-LCL
442 [correspondence coupling](#) during DJF is much stronger [than the correlation from SM₁](#)~~that the SM₁ coupling~~, and
443 DRY exhibits regions of stronger EF-LCL correspondence than CTRL, however the differences are
444 not statistically significant over much of the domain. A key difference between the flux tower and
445 model simulation estimated $K\tau$ is the depth of the SM. The measurement depth at the tower sites are
446 5cm and 10cm for Adelaide River and Howard Springs respectively, while the model surface layer soil
447 moisture is taken from a depth of 0.7 cm. The change in sign of SM₁-LCL $K\tau$ from SON (Figures [8b](#)
448 [and 8d7b-and-7d](#)) to DJF (Figures [8a and 8c7a-and-7e](#)) demonstrates that applying Equation (4) to SM₁
449 and the LCL doesn't always capture the coupling between the land and the atmosphere during periods
450 where deep SM and transpiration dominate the ET flux.

451
452 In short, our results demonstrate that the simulated surface layer soil moisture cannot adequately
453 capture the SM-LCL association during both DJF and SON. The significant contributions of
454 transpiration to the total ET fluxes (especially during SON) are responsive to perturbations in SM_{r_z} and
455 not SM₁.

456

457 **4.6 Proposed Association strength definition: SM_{r_z}-LCL**

458 The definition of land-atmosphere coupling using land surface moisture states and fluxes must
459 encompass the relevant physical mechanisms. Previously, Ferguson et al. (2012) was limited to using
460 SM_1 in deriving $K\tau$ because the AMSR-E (or other microwave) SM measurements typically measure
461 to depths less than a few centimeters beneath the soil surface. Computing $K\tau$ between SM_1 and the
462 LCL incorporates the surface layer soil moisture that is important for surface evaporation from the
463 soil. Therefore the DJF coupling (or other periods where the ET is largely comprised of soil
464 evaporation) should be adequately defined using SM_1 . $K\tau$ computed from SM_1 neglects SM_{rz}
465 variations that drive transpiration during the initial increase in precipitation following the dry season
466 and therefore may not fully encompass the extent of land-atmosphere associations. Acknowledging
467 the importance of transpiration during the Northern Australian wet season, we further evaluate the
468 land-atmosphere association by computing $K\tau$ between the vertically averaged SM_{rz} and the LCL. As
469 opposed to remotely sensed SM from AMSR-E (or other satellite products), the use of simulated SM
470 facilitates the estimation of SM_{rz} . Applying Equation (4) using SM_{rz} imposes a different set of
471 problems, as the rooting depth is model dependent and generally only approximately known. There is
472 substantial evidence that eucalypts have rooting depths exceeding 20 meters (Schenk and Jackson
473 2002), however neither CLM4 nor the direct observations in this study extend that deep. Due to these
474 limitations, SM_{rz} is computed as the weighted mean of the SM observations at 10, 40, and 100cm for
475 the Howard Springs site. We assume that the SM_{rz} consists of the soil layers between the surface and a
476 depth of 1m, as greater than 90% of the prescribed roots in CLM4 are within 1m of the surface
477 (Oleson et al. 2010). This assumed rooting depth is consistent with the model formulation but not
478 realistic given the rooting depths of eucalypts.

479

480 Figure 98 shows the ensemble median $K\tau$ coupling strength diagnosed between SM_{rz} and the
481 LCL. Comparing Figures 8 and 97 and 8 it is clear that including the portion of SM that partially
482 controls transpiration increases the magnitude of the DJF SM-LCL associations and eliminates the
483 region near 14°S 131°E with statistically insignificant correspondence (Figures 8a and 8c7a and 7e)
484 despite soil evaporation contributing significantly to the simulated ET. Large differences between the
485 SON SM_{rz} -LCL and SM_1 -LCL $K\tau$ are seen south of 15°S and east of 130°E. Despite large regions of
486 statistically significant SON SM_{rz} -LCL $K\tau$ for CTRL (Figure 9b8b) and DRY (Figure 9d8d) regions of

487 insignificant association are prevalent near 13°S 131°E. The flux tower derived SON SM_{rz} -LCL
488 correspondence is insignificant in agreement with the DRY and CTRL results near 13°S 131°E. The
489 similarity between the DRY and CTRL SM_{rz} -LCL $K\tau$ highlights the negligible groundwater impact
490 (Figures [9b and 9d&b-and-8d](#)). Comparing Figures [9b and 9d&b-and-8d](#) with Figure 3b and 3d reveals
491 that despite the impact of groundwater on the mean ET flux over SON, the mean state of the deep SM
492 imparts little influence on the temporal dynamics of SM_{rz} in relation to the LCL. Neglecting the SM
493 beneath the surface layer in the calculation of $K\tau$ results in a weak diagnosed SM-LCL association
494 during SON because transpiration is partly governed by the water availability within the root zone. By
495 defining the association using SM_{rz} it is clear that the land is strongly linked to the LCL during both
496 DJF and SON. The DJF SM-LCL association in CTRL near flux tower sites is stronger when defined
497 in this manner, although both sets of simulations still show SM_{rz} to be statistically associated to the
498 LCL.

499
500 The SM_1 -LCL, and SM_{rz} -LCL $K\tau$ shown in Figures [8 and 97-and-8](#) are the median from
501 ensembles with 32 estimates. The ensembles explicitly use multiple constructions of LCL to sample
502 the possible range atmospheric states given the near surface MERRA and GLDAS estimates, and may
503 lead to uncertain estimates of $K\tau$. The inter-ensemble uncertainty of the $K\tau$ metric is examined to
504 demonstrate the robustness of the results. The standard deviation of the [association coupling strength](#)
505 between SM_{rz} and the LCL and between SM_1 and the LCL among the ensemble members is generally
506 less than 0.15 (Figures [10a-10d&a-8d](#)). The variation among the ensemble members is smaller than
507 the median [K \$\tau\$ coupling strength](#) shown in Figures [8 and 97-and-8](#). The low standard deviation
508 relative to the median demonstrates that the association shown in Figures [8 and 97-and-8](#) is robust in
509 that greater than 83% of the $K\tau$ estimates (assuming they are normally distributed) have a
510 correspondence of the same sign reported in the figures. The [correspondence coupling](#) using SM_1
511 (Figure [10c&e](#)) show larger ensemble uncertainty near the coast centered around 135E compared to the
512 SM_{rz} [association coupling](#) in DJF (Figure [10a&a](#)) and over the Cape York Peninsula in SON (Figures
513 [10b and 10a&b-and-8a](#)). Aside from the region near 15S and 130E during SON, the larger ensemble
514 uncertainty is found when using SM_1 to define the [correspondence coupling strength](#).

515

516 **5 Discussion**

517 The seasonal ET from CTRL, DRY, and the gridded ET products from DJF through SON
518 provide insight into the mechanisms that limit the SON DRY ET. The ET from CTRL and DRY are
519 similar (within +/- 10%) during the large DJF precipitation forcing. The dry season commences
520 between MAM and JJA (Figure 1) resulting in increased vapor pressure deficit (VPD) between the
521 vegetation and the atmosphere and increased photosynthetically active radiation (PAR). The changes
522 in VPD and PAR promote increased transpiration from DJF through MAM, although the actual
523 transpiration is also governed by SM_{rz} . Comparing [Figures 3, 5, and 6](#) ~~Figure 3 and Figure 5~~ indicates
524 that the DRY ET is relatively SM limited and unable to maintain ET similar in magnitude to CTRL
525 and the observationally based estimates during SON. [The SM limitation causes a reduction in the total](#)
526 [ET by limiting the amount of transpiration \(Figure 6d\)](#). Within the model, the soil column-
527 groundwater interactions parameterized in CTRL inhibit the large, ET limiting SM_{rz} reduction present
528 in DRY. In reality the inability of DRY to maintain ET during SON may result from the shallow
529 rooting depths assumed in CLM4. The depths are substantially shallower than the rooting depths of
530 eucalypts. Realistic rooting depth profiles reaching nearly 20 meters in Australia (Schenk and Jackson
531 2002) and corresponding soil layer depths may negate the impact of the parameterized soil column-
532 groundwater impacts current in CLM4.

533
534 The EF-LCL association (Figure [76](#)) is similar for both model configurations despite the mean
535 ET (Figure 3) ~~and~~ SM (Figure 5) [and transpiration fraction \(Figure 6\)](#) differing considerably between
536 CTRL and DRY. The [EF-LCL](#) similarity holds for both DJF and SON despite the differing
537 background soil moisture states between the two periods [and differing contributions of transpiration to](#)
538 [the total ET \(Figure 6\)](#). The results indicate that while the mean ET [and transpiration fraction](#) is a
539 strong function of mean soil moisture, the SM-LCL [association coupling](#) as diagnosed here is
540 insensitive to the background state. The coincidence of the temporal variations in SM, EF, and LCL
541 are demonstrated by the large values of $K\tau$.— These seemingly counterintuitive results may be an
542 artifact of using a rank correlation coefficient to determine the strength of the correspondence. $K\tau$
543 only measures the temporal coincidence of the two time-series while neglecting the magnitude of
544 these variations. Although $K\tau$ is largely independent to the background soil moisture state, alternative
545 definitions of association may not remain as invariant.

546

547 | While association in Figure 76 is largely unaffected by the mean SM state, the mean ET flux is
548 largely derived from deeper SM through transpiration during the onset of the wet season prior to DJF.
549 Correspondence under these conditions is poorly defined using SM_1 . The strong EF-LCL coupling
550 during SON and DJF highlights the inadequacy of coupling diagnosed with SM_1 . The physically
551 improbable SM_1 -LCL coupling varies from positive (Figure 7b5b) to negative (Figure 7a5a) as the wet
552 season is established (Figure 1). Despite the domain mean precipitation increasing from roughly zero
553 to several mm/day during SON, $K\tau$ from SM_1 -LCL exhibits both positive (i.e. 15°S 126°E) and
554 negative (i.e. 15°S 134°E) coupling over this period. The transition from negligible (or positive) to
555 strong land-atmosphere association during the wet season is an artifact resulting from the use of SM_1 .
556 More consistent correspondence in general agreement with the EF-LCL dynamics throughout the wet
557 season exists between SM_{rz} -LCL because transpiration is incorporated into the coupling diagnostic.
558 During SON, the dry surface layer SM is responsible for little ET, with variations in ET not associated
559 with SM_1 . The SM_{rz} -LCL $K\tau$ eliminates the insignificant association around 17°S 128°E exhibited in
560 the SM_1 -LCL association. Despite regions of significant SM_{rz} -LCL association in DRY and CTRL, the
561 Howard Springs data show insignificant SM_{rz} -LCL correspondence during SON. The lack of observed
562 association is possibly related to the inability to sample SM at depths that correspond to the physically
563 relevant rooting depths. The necessity of using SM_{RZ} agrees with Lee et al. (2012) where transpiration
564 was found to limit precipitation variability over tropical regions. The importance of transpiration
565 among the various ET components is not limited to Northern Australia or monsoon regions (Coenders-
566 Gerrits et al. 2014; Schlesinger and Jasechko 2014) highlighting the need to characterize land-
567 atmosphere dynamics using SM well beneath the surface.

568

569 | Statistically determining the association using only near surface variables from land surface
570 model simulations of SM and atmospheric data as done in this study (i.e. Ferguson et al. 2013, Betts
571 2004) is limited due to only examining a part of the full land-atmosphere coupling processes. While
572 the LCL is an important determinant in the formation of precipitation, moisture convergence, upper
573 level inversions, convective available potential energy, wind shear, and many other factors play
574 important roles in the formation of convection. The correspondence diagnosed in this study with
575 Equation (4) is by definition limited in scope to only part of the coupling continuum described in

576 Equation (1). Therefore association defined using these methods provides a necessary but not
577 sufficient condition for strong land-atmosphere interactions between soil moisture and precipitation.

578

579 Our results likely extend to monsoonal regions beyond Northern Australia. GLACE (Koster
580 et al. 2006) revealed multiple areas of strong land-atmosphere coupling coincide with major monsoon
581 systems. The strong coupling during the wet season (September-February) diagnosed using SM_{rz} and
582 $K\tau$ in our results qualitatively agrees with the strong coupling in monsoon regions from GLACE. The
583 dry season antecedent to the large precipitation fluxes induces low evaporation while allowing deeply
584 rooted plants to transpire despite the prolonged dry period. These conditions over Northern Australia
585 (Figures 3 and 4) lead to transpiration dominating the ET flux during the onset of the wet season.
586 Coupling diagnosed using $K\tau$ under these conditions must be defined using SM_{rz} rather than SM_1 to
587 ensure the relevant pathways of the moisture fluxes are not neglected.

588

589 **6 Conclusions**

590 The land-atmosphere coupling strength is analyzed utilizing ensembles of land surface
591 simulations and near surface atmospheric data. Using four forcing datasets, ensembles of CLM
592 simulations over Northern Australia are performed, using configurations that either include or neglect
593 soil column-groundwater interactions. The seasonal dynamics of the simulated SM_1 is insensitive to
594 the mean soil moisture state and all simulations compare favorably with the AMSR-E soil moisture
595 product. Further, the simulated ET from December to February is similar between the CTRL and DRY
596 runs, with both configurations largely consistent with the DJF ET estimated from three gridded ET
597 products.

598

599 The strength of the land-atmosphere association is diagnosed between both SM_1 and EF from
600 the simulations and the LCL as calculated from the near surface atmospheric state. During the peak
601 wet season strong SM_1 -LCL and EF-LCL associations are shown. The wet season onset (SON) shows
602 strong EF-LCL association that contrasts the weak SM_1 -LCL association demonstrating the SON
603 coupling is not properly characterized with SM_1 . The land-atmosphere interactions during periods
604 with non-negligible transpiration necessitates the use of root zone soil moisture instead of the surface
605 soil moisture to properly capture the physical processes. Properly defining the association with SM_{rz}

606 | differs considerably from the SM_1 diagnosed association and shows strong correspondence associations
607 throughout the wet season. The SM_{rz} -LCL association is consistent with that from EF-LCL. It should
608 be noted that these associations are a necessary but not sufficient condition to diagnose full land-
609 atmosphere coupling.

610

611 | Our results also show that the statistically diagnosed land-atmosphere correspondence in our
612 offline simulation coupling is insensitive to the mean vertical profile of soil moisture. It is however,
613 sensitive to the depth of the soil column considered. The implication of our findings therefore
614 indicates a need to include the root zone in order capture periods when the ET is dominated by
615 transpiration. We recommend that future studies of land-atmosphere coupling should include
616 groundwater and focus on root zone soil moisture rather than surface layer soil moisture.

617

618

619 **Acknowledgments**

620 We acknowledge support from the Australian Research Council Super Science scheme
621 (FS100100054). AJP was also supported by the Australian Research Council Centre of Excellence for
622 Climate System Science (CE110001028). JPE was supported by an Australian Research Council
623 Future Fellowship (FT110100576). The GLDAS data used in this study were acquired as part of the
624 NASA's Earth-Sun System Division and archived and distributed by the Goddard Earth Sciences
625 (GES) Data and Information Services Center (DISC) Distributed Active Archive Center (DAAC). We
626 also thank Diego Miralles for providing the GLEAM ET product.

627

628

629 **References**

630 Betts, A. K. 2009: Land-Surface-Atmosphere Coupling in Observations and Models. *J. Adv. Model.*
631 *Earth Syst.*, **1 (3)**, doi:10.3894/JAMES.2009.1.4.

632
633 Betts, A. K., J. H. Ball, A. C. M. Beljaars, M. J. Miller, and P. A. Viterbo. 1996: The Land Surface-
634 atmosphere Interaction: A Review Based on Observational and Global Modeling Perspectives, *J.*
635 *Geophys. Res-Atmos.*, **101 (D3)**, 7209–7225. doi:10.1029/95JD02135.

636
637 Betts, A. K., B. Helliker, and J. Berry, 2004: Coupling Between CO₂, Water Vapor, Temperature, and
638 Radon and Their Fluxes in an Idealized Equilibrium Boundary Layer over Land, *J. Geophys. Res.-*
639 *Atmos.*, **109 (D18)**, doi:10.1029/2003JD004420.

640
641 Beringer, J., 2013a: Adelaide River OzFlux tower site OzFlux: Australian and New Zealand Flux
642 Research and Monitoring hdl: 102.100.100/14228

643
644 Beringer, J., 2013b: Howard Springs OzFlux tower site. OzFlux: Australian and New Zealand Flux
645 Research and Monitoring. hdl: 102.100.100/14234

646
647 Bosilovich, M. G., J. Chen, F. R. Robertson, and R. F. Adler, 2008: Evaluation of Global Precipitation
648 in Reanalyses, *J. Appl. Meteor. Climatol.*, **47 (9)**, 2279–2299.

649
650 Coenders-Gerrits, A. M. J., van der Ent, R. J., Bogaard, T. A., Wang-Erlandsson, L.,
651 Hra-chowitz, M., and Savenije, H. H. G., 2014: Uncertainties in transpiration estimates,
652 *Nature*, **506**, doi:10.1038/nature12925.

653
654 Decker, M., and X. Zeng. 2009: Impact of Modified Richards Equation on Global Soil Moisture
655 Simulation in the Community Land Model (CLM3.5), *J. Adv. Model. Earth Syst.*, **1 (3)**,
656 doi:10.3894/JAMES.2009.1.5.

657
658 Decker M., A. Pitman, J. P. Evans, 2013: Groundwater constraints on simulated transpiration

659 variability over Southeastern Australian forests, *J. Hydrometeor.*, **14**, 543–559.
660

661 Decker M., A. Pitman, J. P. Evans, 2014: Applying scaled vegetation greenness metrics to constrain
662 simulated transpiration anomalies: A study over Australia, *J. Hydrometeor.*, **15**, 1607–1623.
663

664 Dirmeyer, Paul A., Xiang Gao, Mei Zhao, Zhichang Guo, Taikan Oki, Naota Hanasaki, 2006: GSWP-
665 2: Multimodel Analysis and Implications for Our Perception of the Land Surface, *Bull. Amer. Meteor.*
666 *Soc.*, **87**, 1381–1397, doi: <http://dx.doi.org/10.1175/BAMS-87-10-1381>
667

668 Draper, C. S., J. P. Walker, P. J. Steinle, R. A.M. de Jeu, and T. R.H. Holmes, 2009: An Evaluation of
669 AMSR-E Derived Soil Moisture over Australia, *Remote Sens. Environ.*, **113** (4), 703–710.
670

671 Eamus, D., and R. Froend. 2006: Groundwater-dependent Ecosystems: The Where, What and Why of
672 GDEs, *Aust. J. Bot.*, **54** (2), 91–96.
673

674 Evans, J. P., A. J. Pitman, and F. T. Cruz, 2011: Coupled atmospheric and land surface dynamics over
675 southeast Australia: A review, analysis and identification of future research priorities. *International*
676 *Journal of Climatology*, **31**, 1758–1772, doi:10.1002/joc.2206.
677

678 Fan, Y., G. Miguez-Macho, C. P. Weaver, R. Walko, and A. Robock, 2007: Incorporating Water Table
679 Dynamics in Climate Modeling: 1. Water Table Observations and Equilibrium Water Table
680 Simulations, *J. Geophys. Res.-Atmos.*, **112** (D10), doi:10.1029/2006JD008111.
681

682 Ferguson, C. R., and E. F. Wood, 2009: Observing land–atmosphere interaction globally with satellite
683 remote sensing, Proc. Earth Observation and Water Cycle Science Symp., Frascati, Italy, European
684 Space Agency, P17.
685

686 Ferguson, C. R., E. F. Wood, and R. K. Vinukollu, 2012: A Global Intercomparison of Modeled and
687 Observed Land-Atmosphere Coupling, *J. Hydrometeor.*, **13** (3), 749–784, doi:10.1175/JHM-D-11-
688 0119.1.

689
690 Gedney, N., and P. M. Cox, 2003: The Sensitivity of Global Climate Model Simulations to the
691 Representation of Soil Moisture Heterogeneity, *J. Hydrometeor.*, **4** (6), 1265–1275.
692
693 Gentine, P., D. Entekhabi, and J. Polcher, 2011: The Diurnal Behavior of Evaporative Fraction in the
694 Soil–Vegetation–Atmospheric Boundary Layer Continuum, *J. Hydrometeor.*, **12**, 1530-1546.
695
696 Gentine, P., A. A. M. Holtslag, F. D'Andrea, and M. Ek, 2013: Surface and Atmospheric Controls on
697 the Onset of Moist Convection over Land. *J. Hydrometeor.*, **14**, 1443–1462.
698
699 Guo, Z., and Coauthors, 2006: GLACE: The Global Land–Atmosphere Coupling Experiment. Part II:
700 Analysis. *J. Hydrometeor.*, **7**, 611–625, doi: <http://dx.doi.org/10.1175/JHM511.1>.
701
702 Hirsch, A., J. Kala, A. J. Pitman, C. Carouge, J. P. Evans, V. Haverd, and D. Mocko, 2013: Impact of
703 Land Surface Initialisation Approach on Sub-seasonal Forecast Skill: A Regional Analysis in the
704 Southern Hemisphere, *J. Hydrometeor.*, under review.
705
706 Huffman, G. J., D. T. Bolvin, E. J. Nelkin, D. B. Wolff, R. F. Adler, G. Gu, Y. Hong, K. P. Bowman,
707 and E. F. Stocker, 2007: The TRMM Multisatellite Precipitation Analysis (TMPA): Quasi-Global,
708 Multiyear, Combined-Sensor Precipitation Estimates at Fine Scales, *J. Hydrometeor.*, **8** (1), 38–55.
709 doi:10.1175/JHM560.1.
710
711 Jimenez, C., and Coauthors, 2011: Global Intercomparison of 12 Land Surface Heat Flux Estimates, *J.*
712 *Geophys. Res.*, **116**, D02102, doi:[10.1029/2010JD014545](http://dx.doi.org/10.1029/2010JD014545).
713
714 Jones, D. A., W. Wang, and R. Fawcett, 2009: High-quality spatial climate data-sets for Australia, *J.*
715 *Aust. Meteor. Oceanogr.*, **58**, 233-248.
716
717 Jung, M., and Coauthors, 2010: Recent Decline in the Global Land Evapotranspiration Trend Due to
718 Limited Moisture Supply, *Nature*, **467**, 951–954, doi:10.1038/nature09396.

719
720 Koster, R. D., M. J. Suarez, and M. Heiser. 2000: Variance and Predictability of Precipitation at
721 Seasonal-to-Interannual Timescales, *J. Hydrometeor.*, **1** (1), 26–46.
722
723 Koster, R. D., and M. J. Suarez, 2003: Impact of Land Surface Initialization on Seasonal Precipitation
724 and Temperature Prediction, *J. Hydrometeor.*, **4** (2), 408–423.
725
726 Koster, R. D., and Coauthors, 2006: GLACE: The Global Land–Atmosphere Coupling Experiment.
727 Part I: Overview. *J. Hydrometeor.*, **7**, 590–610.
728
729 Koster, R. D., Z. Guo, R. Yang, P. A. Dirmeyer, K. Mitchell, and M. J. Puma, 2009: On the Nature of
730 Soil Moisture in Land Surface Models, *J. Clim.*, **22**, 4322–4335.
731
732 Koster, R. D., and Coauthors, 2011: The Second Phase of the Global Land-Atmosphere Coupling
733 Experiment: Soil Moisture Contributions to Subseasonal Forecast Skill, *J. Hydrometeor.*, **12** (5), 805–
734 822. doi:10.1175/2011JHM1365.1.
735
736 Lee, J.-E., and Coauthors, 2012: Reduction of tropical land region precipitation variability via
737 transpiration, *Geophys. Res. Lett.*, **39**, L19704, doi:10.1029/2012GL053417.
738
739 Lintner, B. R. and J. D. Neelin, 2009: Soil Moisture Impacts on Convective Margins. *J. Hydrometeor.*,
740 **10**, 1026–1039.
741
742 Lintner, B. R., P. Gentine, K. L. Findell, F. D’Andrea, A. H. Sobel, and G. D. Salvucci, 2013: An
743 Idealized Prototype for Large-Scale Land–Atmosphere Coupling. *J. Climate*, **26**, 2379–2389.
744
745 Lo, M.-H., and J. S. Famiglietti, 2010: Effect of water table dynamics on land surface hydrologic
746 memory, *J. Geophys. Res.*, **115**, D22118, doi:[10.1029/2010JD014191](https://doi.org/10.1029/2010JD014191).
747
748 Meng X.H., Evans J.P., McCabe M.F. (2014a) The Impact of Observed Vegetation Changes on Land–

749 Atmosphere Feedbacks During Drought. *J Hydrometeor.*, **15**, 759–776. doi: 10.1175/JHM-D-13-
750 0130.1
751

752 Meng, X. H., Evans, J. P. and McCabe, M. F. (2014b): The influence of inter-annually varying albedo
753 on regional climate and drought, *Clim Dyn*, 42(3-4), 787–803, doi:10.1007/s00382-013-1790-0.
754

755 Miralles, D. G., R. A. M. De Jeu, J. H. Gash, T. R. H. Holmes, and A. J. Dolman. 2011: Magnitude and
756 Variability of Land Evaporation and Its Components at the Global Scale, *Hydrol. Earth Syst. Sc.*, **15**
757 **(3)**, 967–981, doi:10.5194/hess-15-967-2011.
758

759 Miralles, D. G., T. R. H. Holmes, R. A. M. De Jeu, J. H. Gash, A. G. C. A. Meesters, and A. J.
760 Dolman, 2010: Global Land-surface Evaporation Estimated from Satellite-based Observations,
761 *Hydrol. Earth Syst. Sc.*, **7 (5)**, 8479–8519. doi:10.5194/hessd-7-8479-2010.
762

763 Mu, Q., F. A. Heinsch, M. Zhao, and S. W. Running, 2007: Development of a global
764 evapotranspiration algorithm based on MODIS and global meteorology data, *Remote Sens. Environ.*,
765 **111**, 519-536, doi:10.1016/j.rse.2007.04.015.
766

767 Mu, Q., L. A. Jones, J. S. Kimball, K. C. McDonald and S. W. Running, 2009: Satellite assesment of
768 land surface evapotranspiration for the pan-Arctic domain, *Water Resour. Res.*, **45**,
769 doi:10.1029/2008WR007189.
770

771 Niu, G.-Y., Z.-L. Yang, R. E. Dickinson, L. E. Gulden, and H. Su, 2007: Development of a Simple
772 Groundwater Model for Use in Climate Models and Evaluation with Gravity Recovery and Climate
773 Experiment Data, *J. Geophys. Res.-Atmos.*, **112 (D7)**, doi:10.1029/2006JD007522.
774

775 Njoku, E.G., T.J. Jackson, V. Lakshmi, T.K. Chan, and S.V. Nghiem, 2003: Soil Moisture Retrieval
776 from AMSR-E, *Geoscience and Remote Sensing, IEEE Transactions*, **41 (2)**, 215–229,
777 doi:10.1109/TGRS.2002.808243.
778

779 Oleson, K., and Coauthors, 2010: Technical Description of Version 4.0 of the Community Land Model
780 (CLM), [Http://dx.doi.org/10.5065/D6FB50WZ](http://dx.doi.org/10.5065/D6FB50WZ),
781 <http://nldr.library.ucar.edu/repository/collections/TECH-NOTE-000-000-000-848>.
782

783 Pielke, R. A., and Coauthors, 2011: Land Use/land Cover Changes and Climate: Modeling Analysis
784 and Observational Evidence, *WIREs. Clim.*, **2 (6)**, 828–850. doi:10.1002/wcc.144.
785

786 Pitman, A. J. 2003: The Evolution of, and Revolution in, Land Surface Schemes Designed for Climate
787 Models, *Int. J. Climatol.*, **23 (5)**, 479–510, doi:10.1002/joc.893.
788

789 Press, W. H., B. P. Flannery, S. A. Teukolsky, and W. T. Vetterling, 1992: Nonparametric or rank
790 correlation, Numerical Recipes in C: The Art of Scientific Computing, L. Cowles and A. Harvey, Eds.,
791 2nd ed. Cambridge University Press, 639–644.
792

793 Qian, T., A. Dai, K. E. Trenberth, and K. W. Oleson. 2006: Simulation of Global Land Surface
794 Conditions from 1948 to 2004. Part I: Forcing Data and Evaluations, *J. Hydrometeor.*, **7 (5)**, 953–975,
795 doi:10.1175/JHM540.1.
796

797 Rodell, M., and Coauthors, 2004: The Global Land Data Assimilation System, *Bull. Amer. Meteor.*
798 *Soc.*, **85 (3)**, 381–394, doi:10.1175/BAMS-85-3-381.
799

800 Santanello, J. A., C. D. Peters-Lidard, and S. V. Kumar, 2011: Diagnosing the Sensitivity of Local
801 Land-Atmosphere Coupling via the Soil Moisture-Boundary Layer Interaction, *J. Hydrometeor.*, **12**
802 **(5)**, 766–786, doi:10.1175/JHM-D-10-05014.1.
803

804 Schenk, H. J., and R. B. Jackson, 2002: The Global Biogeography of Roots, *Ecol. Monographs*, **73**,
805 311-328.
806

807 Schlesinger, W. H. and Jasechko, S., 2014: Transpiration in the global water cycle, *Agr. Forest*
808 *Meteorol.*, **189–190**, 115–117, doi:10.1016/j.agrformet.2014.01.011.

809

810 Seneviratne, S. I., T. Corti, E. L. Davin, M. Hirschi, E. B. Jaeger, I. Lehner, B. Orlowsky, and A. J.
811 Teuling, 2010: Investigating Soil Moisture-climate Interactions in a Changing Climate: A Review,
812 *Earth-Science Reviews*, **99**, 125–161, doi:10.1016/j.earscirev.2010.02.004.

813

814 Small, E. E., and S. A. Kurc, 2003: Tight Coupling Between Soil Moisture and the Surface Radiation
815 Budget in Semiarid Environments: Implications for Land-atmosphere Interactions, *Water Resour. Res.*,
816 **39** (10), doi:10.1029/2002WR001297.

817

818 Taylor, C.r M., and R. J. Ellis, 2006: Satellite Detection of Soil Moisture Impacts on Convection at the
819 Mesoscale, *Geophys. Res. Lett.*, **33** (3), doi:10.1029/2005GL025252.

820

821 Vergnes, J.-P., B. Decharme, R. Alkama, E. Martin, F. Habets, and H. Douville, 2012: A Simple
822 Groundwater Scheme for Hydrological and Climate Applications: Description and Offline Evaluation
823 over France, *J. Hydrometeor.*, **13** (4), 1149–1171, doi:10.1175/JHM-D-11-0149.1.

824

825 Westra, D., G. J. Steeneveld, and A. A. M. Holstag, 2012: Some Observational Evidence for Dry Soils
826 Supporting Enhanced Relative Humidity at the Convective Boundary Layer Top, *J. Hydrometeor.*, **13**,
827 1347-1358.

828

829 Williams, J. L., and R. M. Maxwell, 2011: Propagating Subsurface Uncertainty to the Atmosphere
830 Using Fully Coupled Stochastic Simulations, *J. Hydrometeor.*, **12** (4), 690–701,
831 doi:10.1175/2011JHM1363.1.

832

833 Yu, Z., Da. Pollard, and L. Cheng, 2006: On Continental-scale Hydrologic Simulations with a Coupled
834 Hydrologic Model, *J. Hydrology*, **331**, 110–124, doi:10.1016/j.jhydrol.2006.05.021.

835

836 Zeng, X., and M. Decker, 2009: Improving the Numerical Solution of Soil Moisture–Based Richards
837 Equation for Land Models with a Deep or Shallow Water Table. *J. Hydrometeor.*, **10**, 308-319.

838

839 Zhang, J., W.-C. Wang, and J. Wei, 2008: Assessing Land-atmosphere Coupling Using Soil Moisture
840 from the Global Land Data Assimilation System and Observational Precipitation, *J. Geophys. Res.-*
841 *Atmos.*, **113**, doi:10.1029/2008JD009807.

842

843 **List of Figures**

844 **Figure 1.** Observations of the domain (18°S-11°S and 120°E-150°E) averaged mean annual cycle of
845 precipitation (P in mm day⁻¹).

846

847 **Figure 2.** (a) The mean normalized (using the first two moments) first layer soil moisture (SM₁) from
848 the CTRL and DRY simulations and the AMSR-E observations. (b) The difference between the mean
849 SM₁ (from all simulations over all months from 2004-2009) and the AMSR-E observations.

850

851 **Figure 3.** The mean ET (Wm⁻²) from the wet season (DJF shown in the left hand column) and the
852 transition between the dry and wet seasons (SON shown in the right hand column). The ensemble
853 mean ET from (a) CTRL over DJF, (b) CTRL over SON, (c) DRY for DJF, (d) DRY from SON, (e)
854 OBS (the mean of three gridded ET products) over DJF, and (f) OBS for SON.

855

856 **Figure 4.** The monthly soil moisture (SM in mm³mm⁻³) from the ensemble mean from CTRL and
857 DRY, AMSR-E, and flux tower measurements (OBS_{tower}) from flux tower sites at (a) Howard Springs
858 at 10cm depth and (b) Adelaide River at 5cm depth. The monthly evapotranspiration (ET Wm⁻²) from
859 CTRL, DRY, the mean of three ET products (OBS_{gridded}) and the measurements at the (c) Howard
860 Springs and (d) Adelaide River flux tower sites.

861

862 **Figure 5.** Spatiotemporal mean soil moisture (mm³mm⁻³) SM as a function of depth (m) for (a) DJF
863 and (b) SON.

864

865 **Figure 6.** The mean transpiration fraction (fraction of total ET from transpiration defined as the ratio
866 of transpiration over total ET) from the wet season (DJF shown in the left hand column) and the
867 transition between the dry and wet seasons (SON shown in the right hand column). The ensemble
868 mean transpiration fraction to total ET from (a) CTRL over DJF, (b) CTRL over SON, (c) DRY for
869 DJF, and (d) DRY from SON.

870 **Figure 6.** The ensemble median Kendall-tau correlation metric (Kτ) between the afternoon time
871 (local) evaporative fraction (EF) and the afternoon computed lifting condensation level (LCL) at from
872 (a) CTRL over DJF, (b) CTRL from SON, (c) DRY over DJF, and (d) DRY from SON. The black-

873 ~~outlined squares in (a)-(d) denote the values from the flux tower sites. Only statistically significant~~
874 ~~(95% confidence level) results are shown in (a)-(d).~~

875

876 **Figure 7.** The ensemble median Kendall-tau correlation metric ($K\tau$) between the afternoon time
877 (local) evaporative fraction ($EF_{\text{morning first layer soil moisture}}(SM_1)$) and the afternoon computed
878 lifting condensation level (LCL) at from (a) CTRL over DJF, (b) CTRL from SON, (c) DRY over DJF,
879 and (d) DRY from SON. The black-outlined squares in (a)-(d) denote the values from the flux tower
880 sites. Only statistically significant (95% confidence level) results are shown in (a)-(d).

881

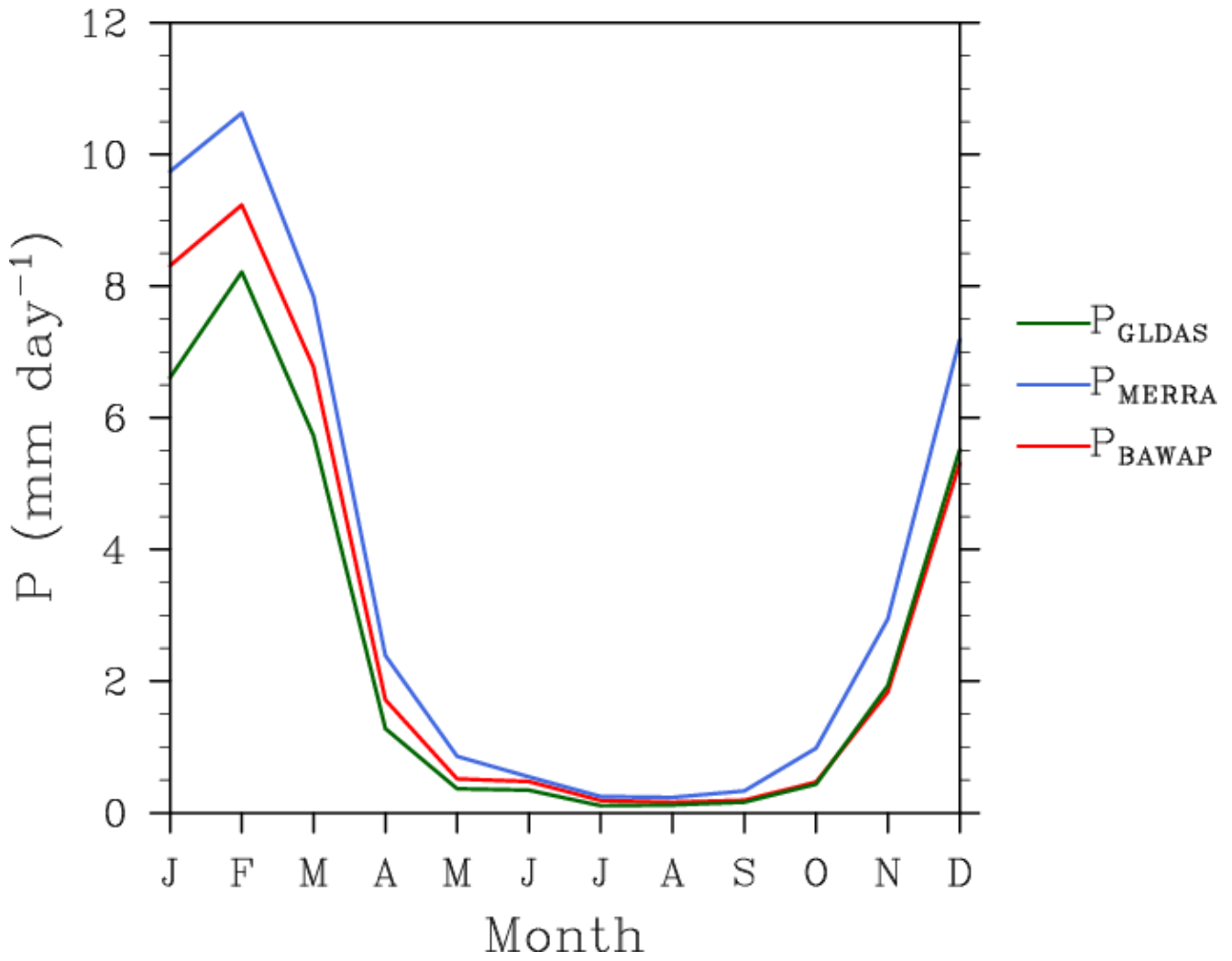
882 **Figure 8.** The ensemble median Kendall-tau correlation metric ($K\tau$) between the morning first
883 layerroot zone soil moisture ($SM_{1,SM_{rz}}$) and the afternoon computed lifting condensation level (LCL)
884 from (a) CTRL over DJF, (b) CTRL from SON, (c) DRY over DJF, and (d) DRY from SON. The
885 black-outlined squares in (a)-(d) denote the values from the Howard Springs flux tower sitesite. Only
886 statistically significant (95% confidence level) results are shown in (a)-(d).

887

888 **Figure 9.** The ensemble median standard deviation of the Kendall-tau correlation metric ($K\tau$)
889 between the morning root zone soil moisture (SM_{rz}) and among the ensemble members between the
890 afternoon computed lifting condensation level (LCL) from (a) CTRL over DJF, (b) CTRL from SON,
891 (c) DRY over DJF, and (d) DRY from SON. The black-outlined squares in (a)-(d) denote the values
892 from the Howard Springs flux tower site. Only statistically significant (95% confidence level) results
893 are shown in (a)-(d)and either the morning root zone soil moisture (SM_{rz}) over (a) DJF, (b) SON, or
894 the morning first layer soil moisture (SM_1) over (c) DJF, and (d) SON.

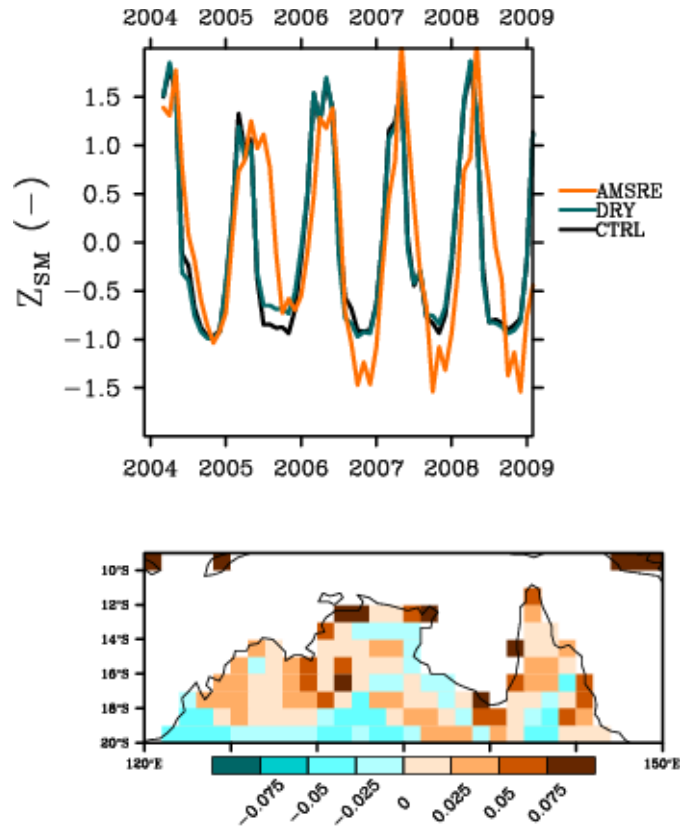
895

896 **Figure 10.** The standard deviation of the Kendall-tau correlation metric ($K\tau$) among the ensemble
897 members between the afternoon computed lifting condensation level (LCL) and either the morning
898 root zone soil moisture (SM_{rz}) over (a) DJF, (b) SON, or the morning first layer soil moisture (SM_1)
899 over (c) DJF, and (d) SON.



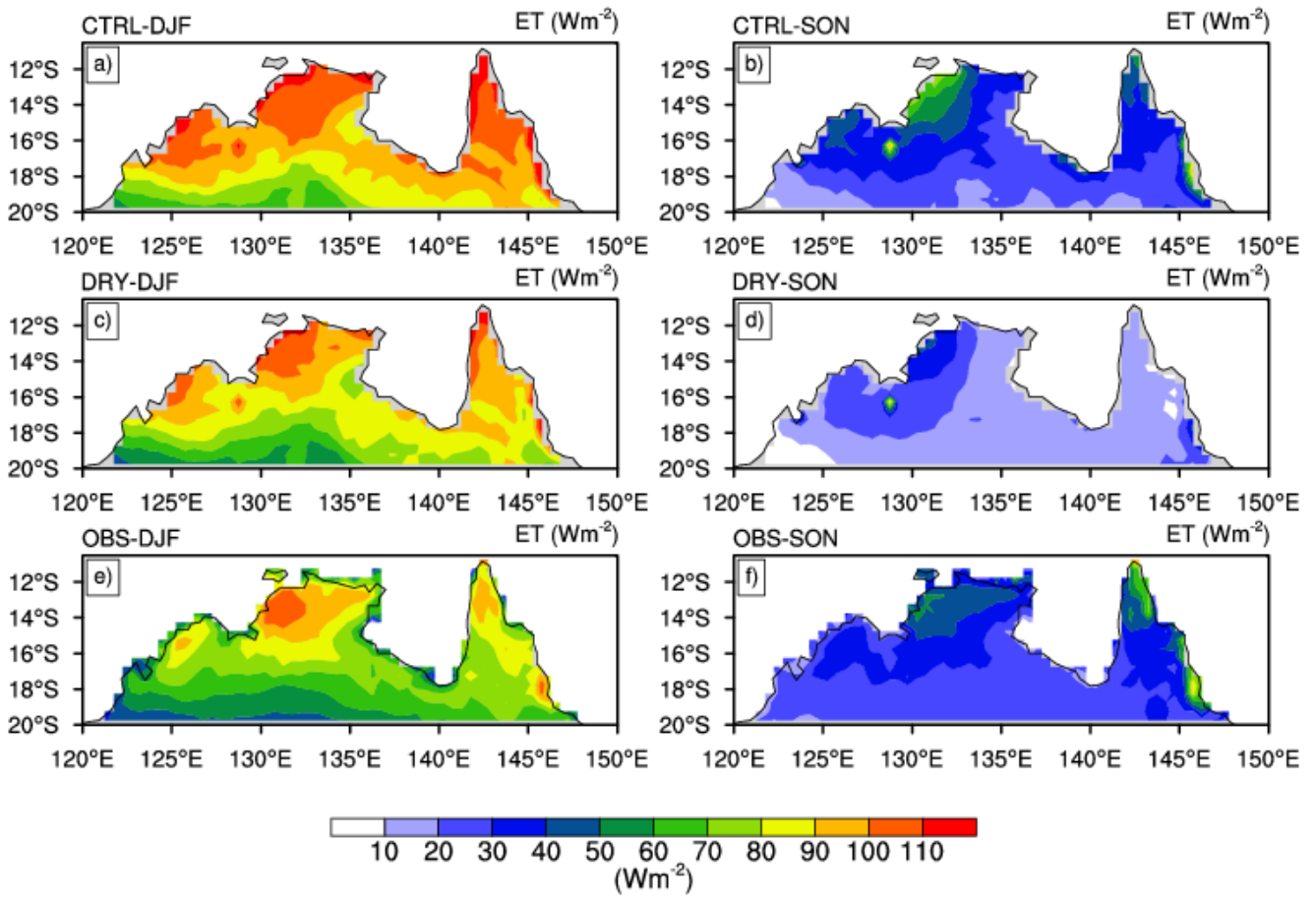
901 | **Figure 1.** Observations of the domain (18°S-11°S and 120°E-150°E) averaged mean annual cycle of (a)
 902 precipitation (P in mm day⁻¹).

903

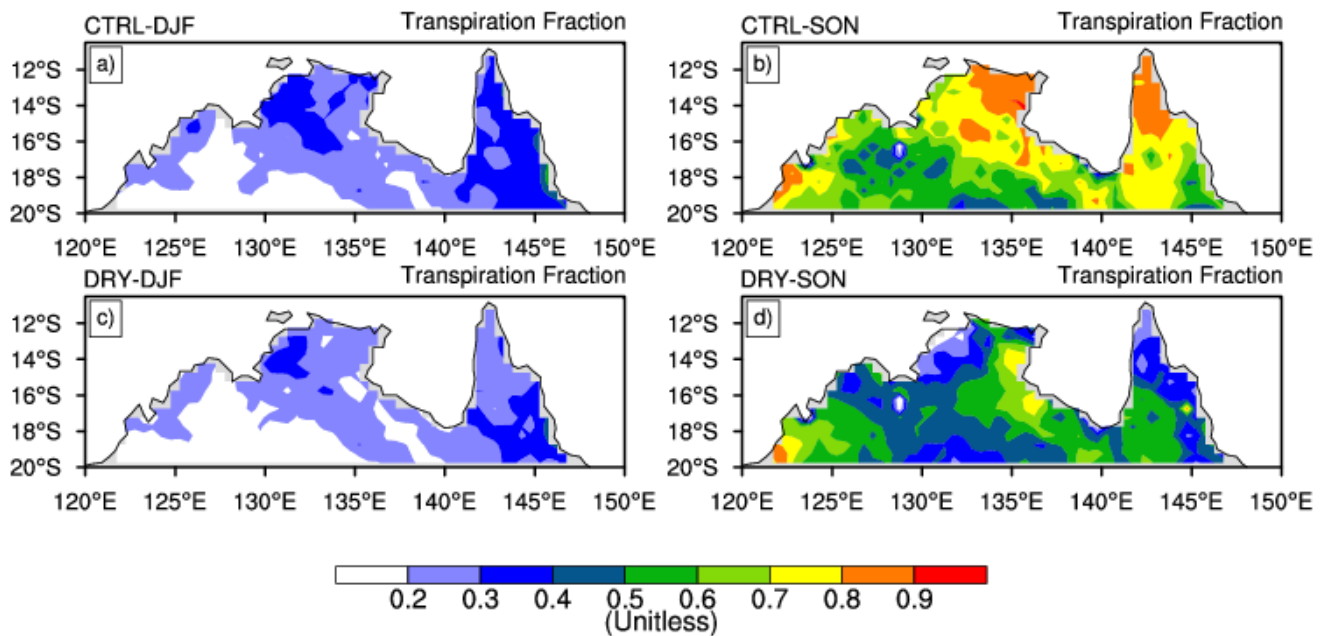


905 |
 906 | **Figure 2.** (a) The mean normalized (using the first two moments) first layer soil moisture (SM_1) from
 907 | the CTRL and DRY simulations and the AMSR-E observations. (b) The difference between the mean
 908 | SM_1 (from all simulations over all months from 2004-2009) and the AMSR-E observations (mm^3mm^{-3}).
 909 |
 910 |

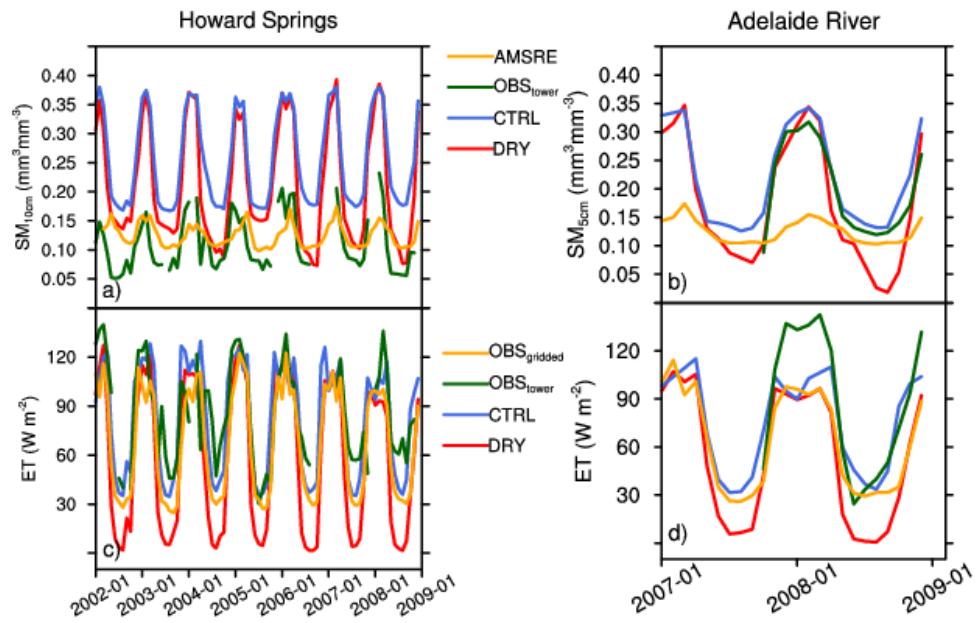
911
912



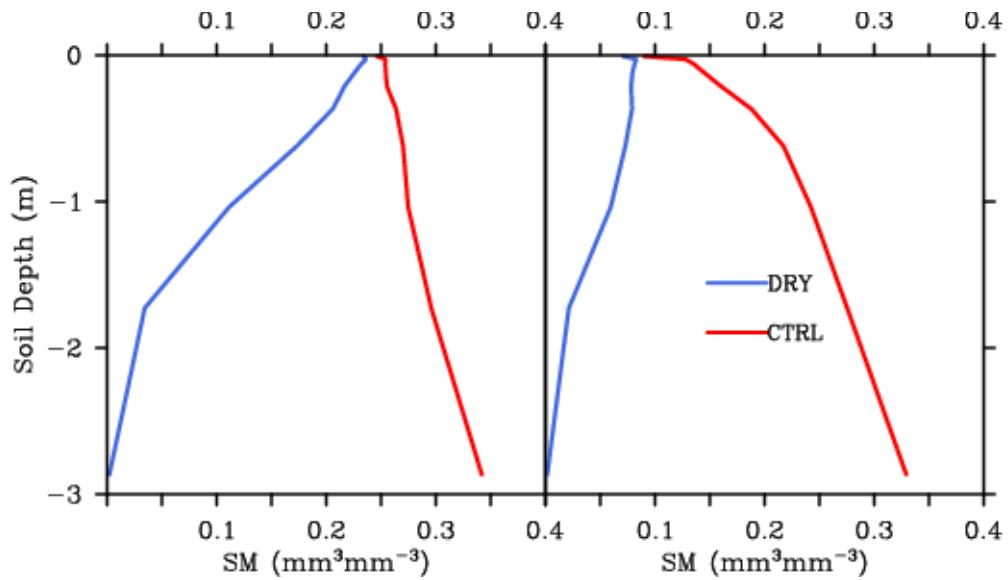
914
915 **Figure 3.** The mean ET (Wm⁻²) from the wet season (DJF shown in the left hand column) and the
916 transition between the dry and wet seasons (SON shown in the right hand column). The ensemble
917 mean ET from (a) CTRL over DJF, (b) CTRL over SON, (c) DRY for DJF, (d) DRY from SON, (e)
918 OBS (the mean of three gridded ET products) over DJF, and (f) OBS for SON.
919



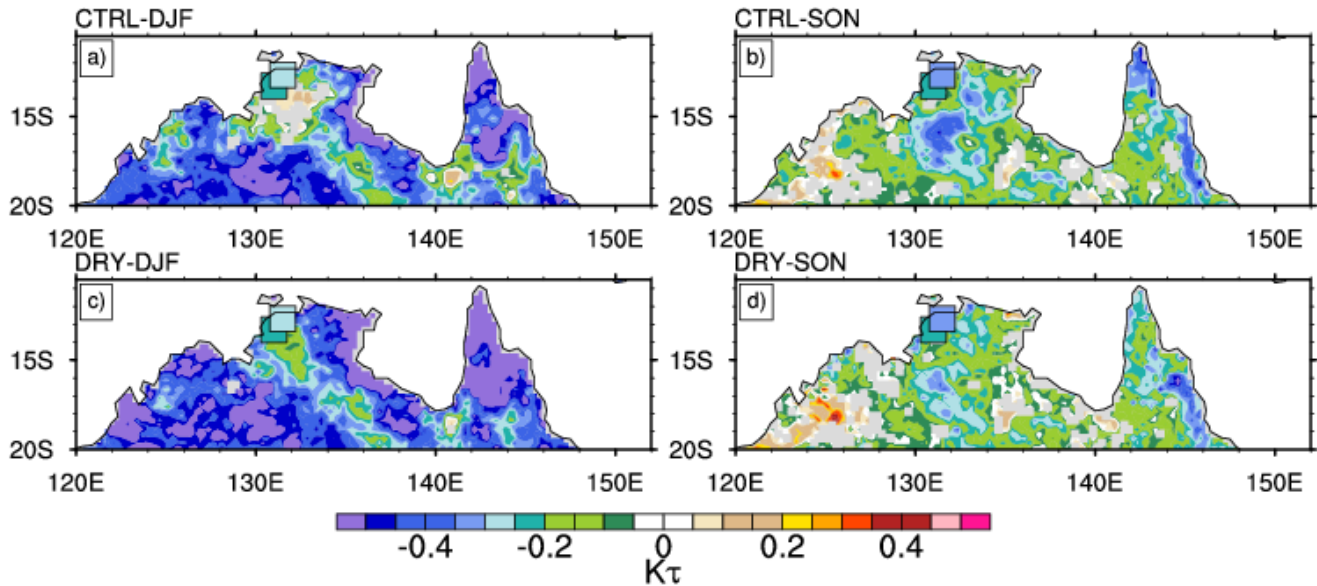
921 | **Figure 4.** The monthly soil moisture (SM in $\text{mm}^3\text{mm}^{-3}$) from the ensemble mean from CTRL and
 922 DRY, AMSR-E, and flux tower measurements ($\text{OBS}_{\text{tower}}$) from flux tower sites at (a) Howard Springs
 923 at 10cm depth and (b) Adelaide River at 5cm depth. The monthly evapotranspiration (ET Wm^{-2}) from
 924 CTRL, DRY, the mean of three ET products ($\text{OBS}_{\text{gridded}}$) and the measurements at the (c) Howard
 925 Springs and (d) Adelaide River flux tower sites.



927 **Figure 5.** Spatiotemporal mean soil moisture ($\text{mm}^3\text{mm}^{-3}$) SM as a function of depth (m) for (a) DJF
 928 and (b) SON.



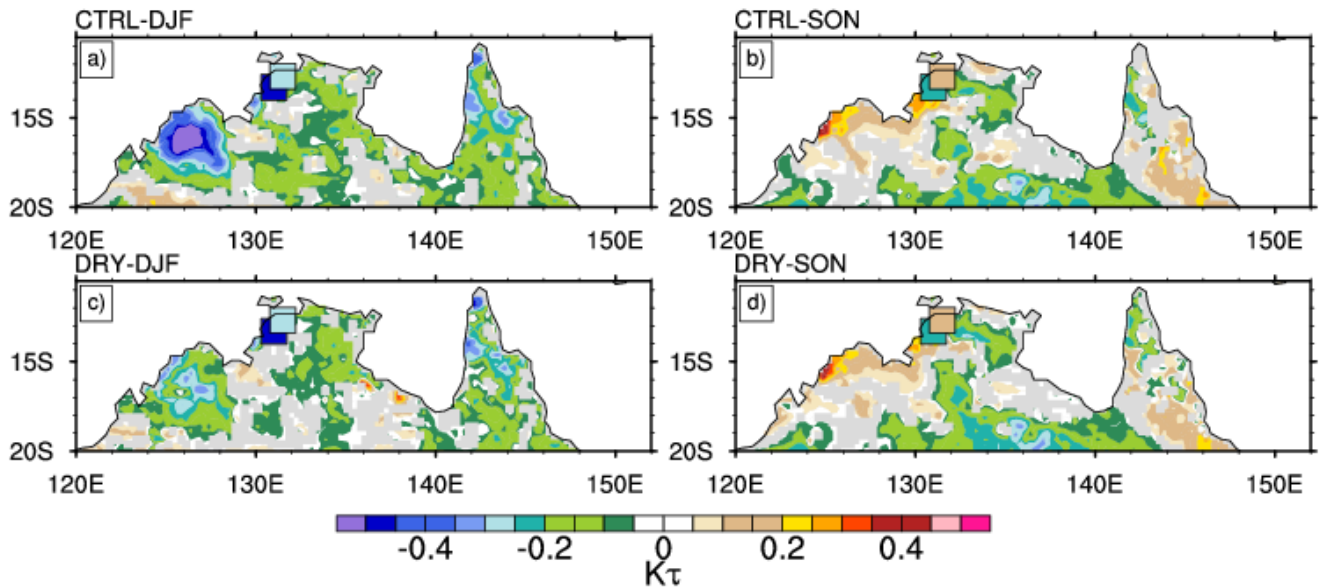
931 **Figure 6.** The mean transpiration fraction (fraction of total ET from transpiration defined as the ratio
 932 of transpiration over total ET) from the wet season (DJF shown in the left hand column) and the
 933 transition between the dry and wet seasons (SON shown in the right hand column). The ensemble
 934 mean transpiration fraction to total ET from (a) CTRL over DJF, (b) CTRL over SON, (c) DRY for
 935 DJF, and (d) DRY from SON.



938 | **Figure 76.** The ensemble median Kendall-tau correlation metric ($K\tau$) between the afternoon time
 939 (local) evaporative fraction (EF) and the afternoon computed lifting condensation level (LCL) at from
 940 (a) CTRL over DJF, (b) CTRL from SON, (c) DRY over DJF, and (d) DRY from SON. The black-
 941 outlined squares in (a)-(d) denote the values from the flux tower sites. Only statistically significant
 942 (95% confidence level) results are shown in (a)-(d).

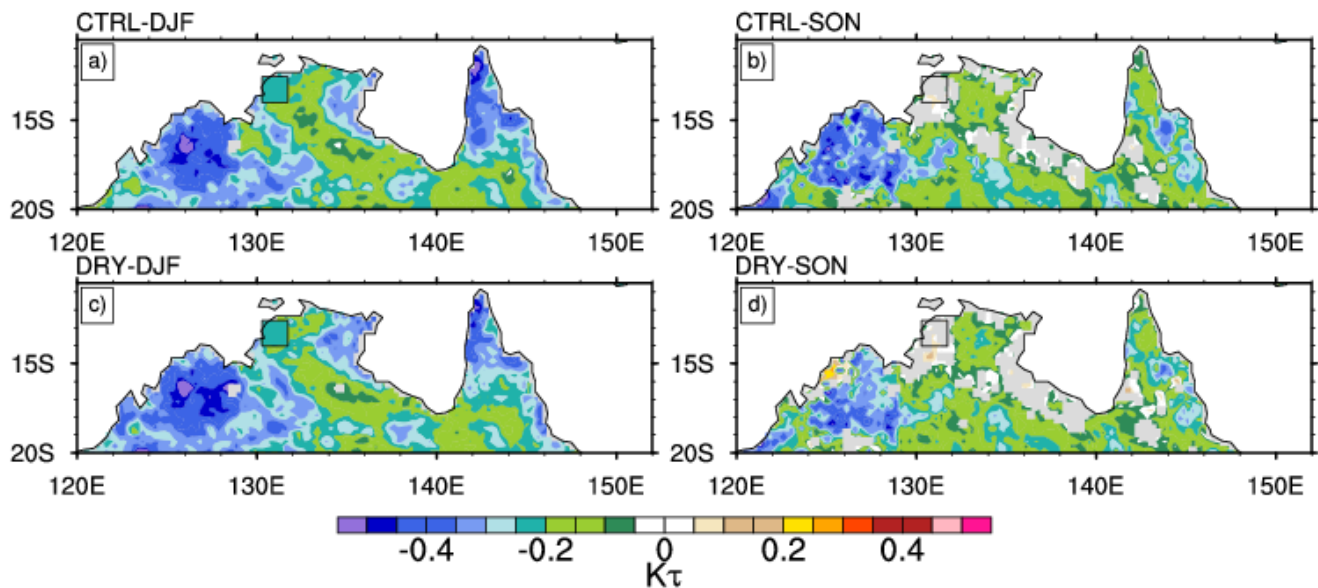
943

944



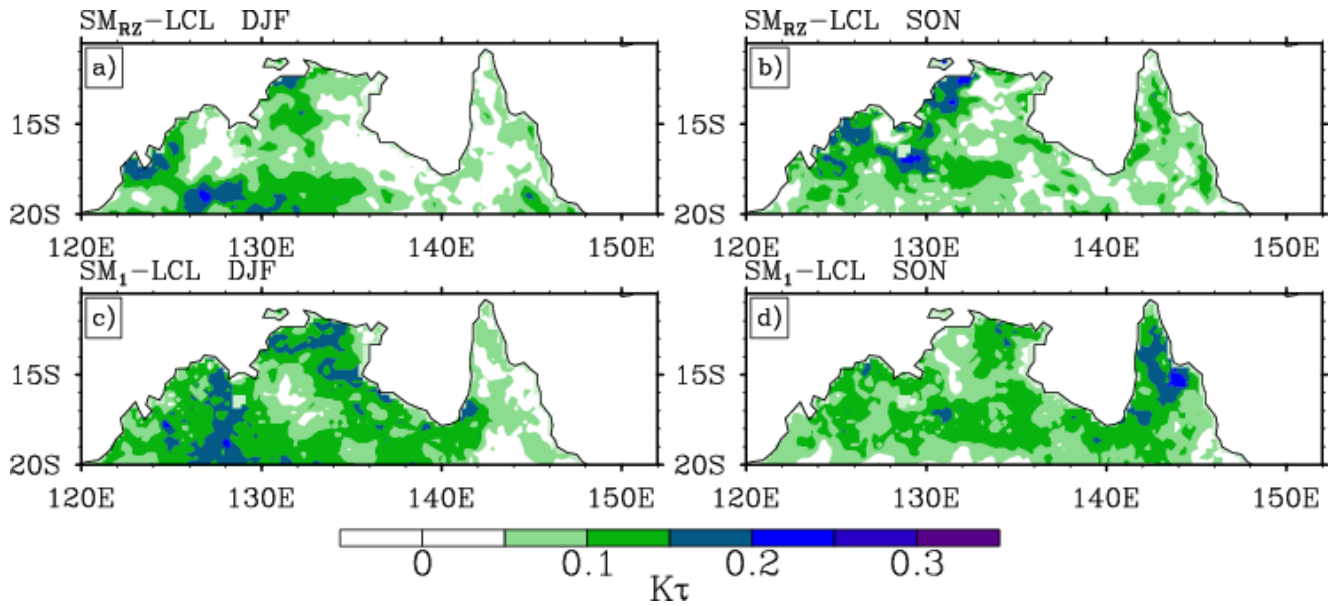
946 | **Figure 87.** The ensemble median Kendall-tau correlation metric ($K\tau$) between the morning first layer
 947 soil moisture (SM_1) and the afternoon computed lifting condensation level (LCL) from (a) CTRL over
 948 DJF, (b) CTRL from SON, (c) DRY over DJF, and (d) DRY from SON. The black-outlined squares in
 949 (a)-(d) denote the values from the flux tower sites. Only statistically significant (95% confidence
 950 level) results are shown in (a)-(d).

951



953 | **Figure 98.** The ensemble median Kendall-tau correlation metric ($K\tau$) between the morning root zone
 954 soil moisture (SM_{rz}) and the afternoon computed lifting condensation level (LCL) from (a) CTRL over
 955 DJF, (b) CTRL from SON, (c) DRY over DJF, and (d) DRY from SON. The black-outlined squares in
 956 (a)-(d) denote the values from the Howard Springs flux tower site. Only statistically significant (95%
 957 confidence level) results are shown in (a)-(d).

958



960
 961 | **Figure 109.** The standard deviation of the Kendall-tau correlation metric ($K\tau$) among the ensemble
 962 members between the afternoon computed lifting condensation level (LCL) and either the morning
 963 root zone soil moisture (SM_{RZ}) over (a) DJF, (b) SON, or the morning first layer soil moisture (SM_1)
 964 over (c) DJF, and (d) SON.